

Pouya Youssefi

Department of Cardiothoracic Surgery,
St. George's Hospital,
London SW17 0QT, UK;
Department of Biomedical Engineering,
King's College London,
London SE1 7EH, UK
e-mail: pyyoussefi@aol.com

Alberto Gomez

Department of Biomedical Engineering,
King's College London,
London SE1 7EH, UK
e-mail: alberto.gomez@kcl.ac.uk

Christopher Arthurs

Department of Biomedical Engineering,
King's College London,
London SE1 7EH, UK
e-mail: christopher.arthurs@kcl.ac.uk

Rajan Sharma

Department of Cardiology,
St. George's Hospital,
London SW17 0QT, UK
e-mail: rajan.sharma@stgeorges.nhs.uk

Marjan Jahangiri

Department of Cardiothoracic Surgery,
St. George's Hospital,
London SW17 0QT, UK
e-mail: marjan.jahangiri@stgeorges.nhs.uk

C. Alberto Figueroa

Department of Biomedical Engineering,
King's College London,
London SE1 7EH, UK;
Departments of Surgery
and Biomedical Engineering,
University of Michigan,
Ann Arbor, MI 48109
e-mail: alberto.figueroa@kcl.ac.uk

Impact of Patient-Specific Inflow Velocity Profile on Hemodynamics of the Thoracic Aorta

Computational fluid dynamics (CFD) provides a noninvasive method to functionally assess aortic hemodynamics. The thoracic aorta has an anatomically complex inlet comprising of the aortic valve and root, which is highly prone to different morphologies and pathologies. We investigated the effect of using patient-specific (PS) inflow velocity profiles compared to idealized profiles based on the patient's flow waveform. A healthy 31 yo with a normally functioning tricuspid aortic valve (subject A), and a 52 yo with a bicuspid aortic valve (BAV), aortic valvular stenosis, and dilated ascending aorta (subject B) were studied. Subjects underwent MR angiography to image and reconstruct three-dimensional (3D) geometric models of the thoracic aorta. Flow-magnetic resonance imaging (MRI) was acquired above the aortic valve and used to extract the patient-specific velocity profiles. Subject B's eccentric asymmetrical inflow profile led to highly complex velocity patterns, which were not replicated by the idealized velocity profiles. Despite having identical flow rates, the idealized inflow profiles displayed significantly different peak and radial velocities. Subject A's results showed some similarity between PS and parabolic inflow profiles; however, other parameters such as $Flow_{asymmetry}$ were significantly different. Idealized inflow velocity profiles significantly alter velocity patterns and produce inaccurate hemodynamic assessments in the thoracic aorta. The complex structure of the aortic valve and its predisposition to pathological change means the inflow into the thoracic aorta can be highly variable. CFD analysis of the thoracic aorta needs to utilize fully PS inflow boundary conditions in order to produce truly meaningful results. [DOI: 10.1115/1.4037857]

1 Introduction

Disease processes such as aneurysm formation and atherosclerosis are largely dependent on hemodynamic factors [1–4]. Flow characteristics play an important role in vascular disease, with effects on endothelial homeostasis [5,6] and on the response of smooth muscle cells and fibroblasts [5,7–9]. Measurement of in vivo hemodynamics can be difficult and invasive [10]. Computational fluid dynamics (CFD) is an ever increasing approach to quantify hemodynamics with high spatial and temporal resolution [11,12]. Computational simulations of blood flow have been used to investigate aneurysm disease [13–15], the design and assessment of vascular devices [16,17], and the planning and outcome prediction of vascular surgeries [18–20]. Due to the complex characteristics of the cardiovascular system, quantification of the intricate flow, velocity, and pressure fields in vascular models

can only be achieved by performing simulations in a patient-specific (PS) manner.

In addition to assumptions regarding the blood rheology, computational grid size, and grid adaptivity, a key aspect in the CFD endeavor is the specification of physiologically accurate boundary conditions [11,21–27]. Typically, most studies have used idealized velocity profiles for the inflow boundary conditions. Such studies have modeled inflow boundary conditions using simple profiles (such as a parabolic, plug, or Womersley), measuring only a few in vivo velocity parameters such as peak velocity, average velocity, or flow rate [28]. Additionally, numerous studies have used inflow data acquired from another source altogether (typically literature), as the utilized imaging modality did not provide blood flow data (e.g., computed tomography).

The need for accurate inflow boundary conditions is particularly important in the thoracic aorta (comprising of the ascending aorta, aortic arch, and descending thoracic aorta). The natural anatomic inlet boundary of the thoracic aorta is the aortic valve, the gatekeeper between the heart and the systemic circulation. The

Manuscript received July 28, 2016; final manuscript received June 9, 2017; published online October 19, 2017. Assoc. Editor: Ender A. Finol.

complexity of this trileaflet valve, along with its ring-like annulus, sinuses, and feeding coronary arteries, may lead to highly intricate flow patterns entering the ascending aorta [29], far from the idealized profiles used traditionally. Furthermore, the aortic valve is prone to an array of pathologies including stenosis (resulting from calcification, degeneration, rheumatic fever, infection), regurgitation (resulting from annuloaortic ectasia, rheumatic fever, infection, connective tissue disorders), and importantly a congenital malformation causing the valve to be bicuspid [30,31]. In fact, bicuspid aortic valve (BAV) is the commonest congenital heart defect affecting 1–2% of the population [32]. These processes all have an effect on the valve structure and morphology, and subsequently to the three-dimensional (3D) shape of the aortic valve outflow velocity pattern. Furthermore, aneurysms of the ascending aorta are often found in combination with aortic valve pathology. There is a strong link between bicuspid aortic valve morphology and ascending aortic aneurysms, as well as between aortic stenosis and poststenotic dilatation of the ascending aorta [33]. Therefore, it might be expected that use of idealized velocity profiles, which do not take into account different aortic valve morphologies, would be inappropriate for the study of thoracic aorta hemodynamics, and yield inaccurate CFD results.

A few studies have investigated the effect of using patient-specific inlet velocity profiles on CFD-simulated hemodynamics of the abdominal aorta [34], carotid arteries [28], cerebral arteries [35], and coronary arteries [36]. Recently, a study by Morbiducci et al. [37] assessed the effect of inlet boundary conditions on the thoracic aorta of a healthy subject, and found that idealized boundary conditions can lead to misleading results. The use of phase-contrast magnetic resonance imaging (MRI) to provide temporally and spatially resolved velocity data has provided a reliable noninvasive method of acquiring patient-specific inflow boundary conditions [38].

The aim of this study is to assess the impact of MRI-based, patient-specific inflow velocity profiles as compared to idealized inflow velocity profiles (based on the patient's flow rate) in CFD simulations of thoracic aortic hemodynamics of both healthy and diseased states. The idealized velocity profiles correspond to parabolic and plug patterns, which are the most commonly used in the literature [28,39]. In this work, we study two subjects: subject A is 31 years old and has a normal trileaflet aortic valve with normal thoracic aortic dimensions; subject B is 52 years old, has aortic valvular stenosis with a bicuspid aortic valve, and a moderately dilated ascending aorta of 4.5 cm diameter. This patient was chosen as the pathology describes a clinical scenario which is commonly faced by cardiothoracic surgeons and cardiologists. The results of this study may have significant implications on the necessity of using patient-specific inflow velocity profiles to study disease states of the thoracic aorta, which often go hand-in-hand with aortic valve pathologies.

2 Methods

2.1 Patient Data. Subjects A and B both underwent magnetic resonance angiography (MRA) to image the entire thoracic aorta, including the head and neck vessels. Gadolinium (0.3 ml/kg; gadodiamide, Omniscan[®], GE Healthcare, Waukesha, WI) was infused with a breath-held 3D fast gradient echo sequence using a Philips Achieva 3T scanner (Philips Medical Systems, Eindhoven, The Netherlands). Slice thickness was 2.0 mm, with 60 sagittal slices per volume. A 344 × 344 acquisition matrix was used with a field of view (FoV) of 35 cm × 35 cm (reconstructed to 0.49 mm × 0.49 mm × 1.00 mm). Other parameters included a repetition time (TR) of 3.9 ms, echo time (TE) of 1.4 ms, and a flip angle of 27 deg.

Time-resolved, two-dimensional (2D) through-plane flow-MRI was acquired orthogonally in the ascending aorta at the sinotubular junction. This is the anatomic location where the round-shaped sinuses of valsalva end and the tubular ascending aorta

begins. Heart rate was 60 bpm (subject A) and 70 bpm (subject B) during which 30 images were reconstructed. Imaging parameters included: TR 4.2 ms, TE 2.4 ms, flip angle 15 deg, FoV 35 cm × 30 cm, acquisition matrix of 152 × 120, slice thickness 8 mm, voxel size 2.3 mm × 2.4 mm × 8 mm (reconstructed to 1.37 mm × 1.36 mm × 8 mm). Data acquisition was carried out with a breath-hold and gated to the cardiac cycle. Average scan times were 20 min. Immediately after scanning, supine measurement of bilateral upper limb blood pressure was performed.

The local research ethics committee approved this study and informed consent was obtained from both subjects.

2.2 Segmentation and Meshing. Three-dimensional geometric models of the thoracic aorta were reconstructed from the MRA data using custom software [40].¹ Centreline paths were defined along the thoracic aorta, innominate artery, left common carotid artery, and left subclavian artery. MRA data were segmented at discrete locations defined by planes perpendicular to these paths [41]. The vessel segmentation procedure was carried out by identifying the vessel boundary through thresholding, where differences in pixel intensity are used to automatically detect vessel boundaries, or by manual interaction. An automated lofting process then interpolated all segmented boundaries, thus creating the three-dimensional model of the arteries. A careful visual comparison was performed by superimposing the computer model with the maximum intensity projections of the MRAs in order to ensure accuracy.

A tetrahedral mesh was created by discretizing the geometric model of the aorta and refined using a combination of global mesh (1 mm), maximum curvature (0.02 mm), and boundary layer refinement. A pulsatile flow simulation was run, followed by a field-based anisotropic mesh refinement [42] operation. This resulted in a final anisotropic mesh consisting of approximately 2,100,000 and 3,100,000 tetrahedral elements and 380,000 and 550,000 nodes for subjects A and B, respectively.

2.3 Finite Element Analysis. Blood flow simulations were carried out using a stabilized finite element formulation to solve equations enforcing conservation of mass (continuity) and balance of linear momentum (Navier–Stokes) for the flow of an incompressible Newtonian fluid with density $\rho = 1.06 \text{ g/cm}^3$ and dynamic viscosity $\mu = 0.04 \text{ Poise}$ [43,44]. The validated in-house code CRIMSON was used for this process [40].¹ Simulations were run using a global residual tolerance 0.001 and time-step size of 0.00025 s. Four to six cardiac cycles were produced until cycle-to-cycle periodicity in the flow and pressure fields was achieved. The last cardiac cycle was used for the purpose of data analysis for each subject.

2.4 Boundary Conditions. The model required the prescription of one inflow and four outflow boundary conditions. The flow-MRI data were used to define the patient-specific inflow velocity profile. This was the main goal of this paper and will be described in detail in Sec. 2.5. The outflow boundary conditions were specified using a coupled-multi-domain method [27,44] in which three-element Windkessel models were coupled to each outflow branch (e.g., innominate artery, left common carotid artery, left subclavian artery, and descending aorta) [45]. The Windkessel model represents the arterial tree beyond the outlet in an intuitive and physiological manner. It comprises of a proximal resistance (R_p), compliance (C), and a distal resistance (R_d) for each outlet. Specification of the Windkessel parameters requires knowledge of flow splits and pressure. Since no flow-MRI data was available for the outflow branches, flow splits were estimated based on the relative cross-sectional area of each outlet. The mean outflow pressure for each outlet was assumed to be equal to that measured by the Dinamap device. The Windkessel parameters

¹<http://www.crimson.software/>

Table 1 Parameter values of the lumped parameter Windkessel boundary conditions. R_p = proximal resistance, R_d = distal resistance, C = capacitance. The units of resistance are 10^3 dynes s/cm^5 . The units of capacitance are 10^{-6} $cm^5/dynes$.

Outlet	Subject A			Subject B		
	R_p	R_d	C	R_p	R_d	C
Descending aorta	0.25	2.14	208	0.17	4.69	109
Brachiocephalic	1.36	9.23	48.3	0.79	18.2	28.2
Left common carotid	2.46	15.3	29.2	1.15	24.9	20.5
Left subclavian	1.74	11.3	39.3	1.29	27.6	18.6

were estimated following the procedure described in Ref. [46]. Table 1 gives the numerical values of these parameters for each branch.

2.5 Patient-Specific Inflow Velocity Profile Boundary Condition. In this study, we present a protocol to impose patient-specific inflow velocity boundary conditions in CFD simulations of thoracic aortic hemodynamics. We compare the results obtained using PS velocity profiles with those obtained using idealized velocity profiles (parabolic and plug) mapped to the flow data of the subject. We refer to the three different inflow velocity profiles as: (i) V_{PS} , (ii) V_{para} , and (iii) V_{plug} .

2.5.1 Flow-MRI. Flow-MRI images of the blood velocity field were acquired just above the aortic valve, at a plane orthogonal to the annulus (ring) of the aortic valve. This plane corresponded to the sinotubular junction, which is the anatomical junction between the sinuses of valsalva, and the ascending aorta. The anatomical limits of the flow-MRI plane were set so that the valve leaflets never crossed into this plane, as this would result in imaging artifacts. This plane matched the inflow face of the aortic model created from the MRA data. Data acquisition was through-plane and the velocity data were acquired over 30 cardiac phases. The encoding velocity constant (V_{enc}) was set to 4000 mm/s in order to ensure no aliasing in subject B with aortic stenosis, and 2500 mm/s in subject A (healthy).

2.5.2 Velocity and Flow Extraction. An in-house software written in MATLAB (The Mathworks Inc., Natick, MA) was used to extract velocity profiles from the flow-MRI images. This software allows the user to extract both the velocity profile V_{PS} and flow rate waveform from the PC-MRI images. The flow rate waveform

was used to assign the two idealized velocity profiles (V_{para} and V_{plug}). The MATLAB code processes velocity data by multiplying the image pixel intensity by the V_{enc} . These velocity data are then segmented as described next.

2.5.3 Segmentation. A graphical interface allows manual segmentation of the lumen boundaries for each of the 30 cardiac phases. This approach enables capturing the movement of the aorta during the cardiac cycle. The segmented boundaries were smoothed using cyclic B-splines to reduce manual delineation inaccuracies of the lumen boundary. A segmentation mask was generated and the velocity profile was obtained by applying the mask to the flow-MRI data.

2.5.4 Mapping of Velocity Profile Onto Inlet Mesh. The inlet face (and corresponding surface mesh) of the MRA-derived aortic geometry was assumed to be fixed both temporally and spatially. This is the result of defining the aortic geometry from a single volumetric image. From a computational perspective, this implies that the aorta is represented as a rigid structure whose boundaries are fixed through the analysis. In contrast, the inflow velocity profiles derived from flow-MRI data have a boundary which changes shape, size, and position with each cardiac phase. Therefore, a 2D mapping of the deforming velocity profiles to the fixed aortic inlet face must be derived to define the inflow velocity field V_{PS} .

The 2D mapping was carried out by defining a rigid alignment followed by a nonrigid adaption between the time-varying lumen boundary in the flow-MR image and the fixed MRA-derived aortic inlet face. Rotational consistency in the rigid alignment was ensured by manually establishing a reference point between the time-varying velocity images and the MRA-derived model. The reference point was chosen to be most anterior point on the aortic wall. The nonrigid deformation was achieved using a coarse B-spline grid, which provided a dense and smooth warp at the boundary and within the cross section of the vessel. The warped velocity profile was then interpolated onto the fixed inlet face mesh (see Fig. 1).

Figure 2 shows 2D and 3D visualizations of the magnitude of patient-specific, plug, and parabolic velocity profiles (first and second rows, respectively) at peak systole. The 3D visualization of the velocity profile was obtained by warping the measured through-plane phase contrast data by a factor of 0.02.

2.6 Quantification of Hemodynamic Indices. Two-dimensional and 3D visualizations of the velocity magnitude, and radial (in-plane) velocity vectors were extracted from the simulation data at

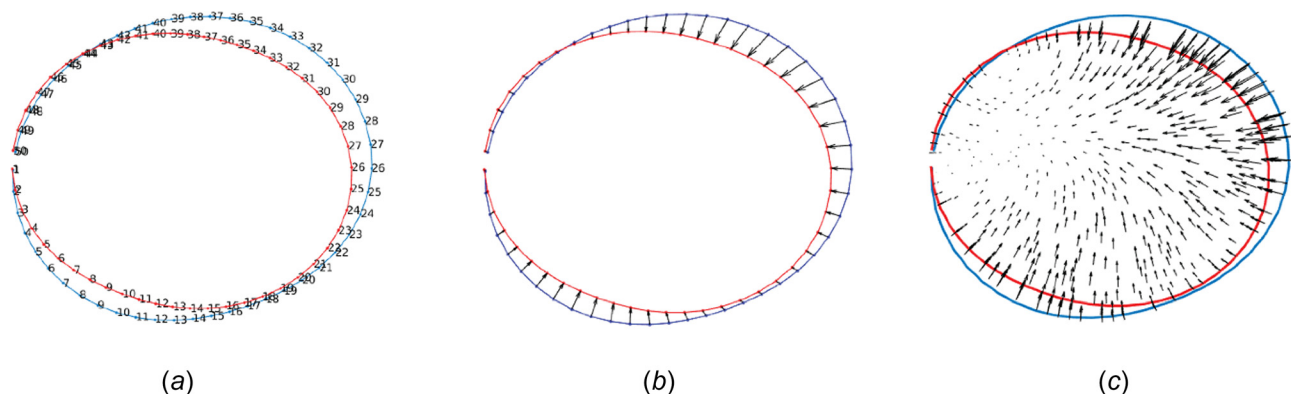


Fig. 1 Geometric mapping between the flow-MRI derived contour (blue: variable in time) and the MRA-derived geometric model contour (red: fixed in time) at the inlet. (a) Rotational alignment between the flow-MRI derived contour and the geometric model inlet is resolved by pointwise correspondence (indicated by numbers) between the two contours. (b) Corresponding points establish a reference deformation between the two contours as indicated by the arrows. (c) The contourwise deformation illustrated in (b) is extended to the entire area of the inlet by using a dense smooth B-spline deformation field (represented by black arrows).

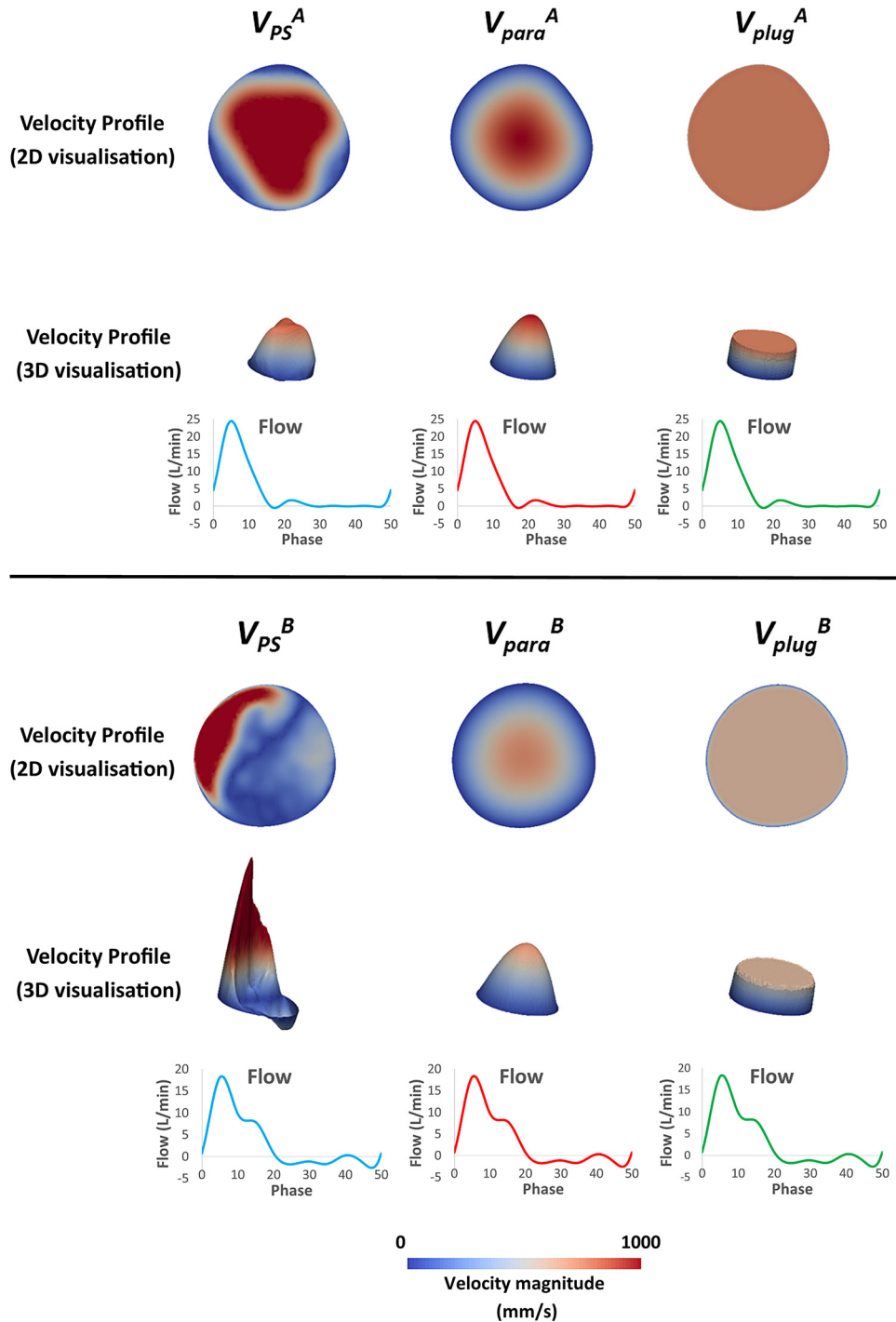


Fig. 2 Inflow boundary conditions. 2D and 3D visualizations of the patient-specific (V_{PS}), parabolic (V_{para}), and plug (V_{plug}) velocity magnitude (first and second rows, respectively) at peak systole. The 3D visualization of the velocity magnitude was obtained by warping the measured through-plane phase contrast data by a factor of 0.02.

three planes along the axis of the thoracic aorta. Plane 1 corresponds to the midascending aorta, plane 2 to the transverse aortic arch, and plane 3 to midthoracic aorta. Radial velocity was assessed by measuring the component of the velocity vectors perpendicular to the long axis of the aorta at each plane. The radial velocities enable the estimation of nonaxial helical flow. Immaterial particle pathlines were calculated from temporally resolved velocity data for the entire thoracic aorta. Hemodynamic quantities were visualized using PARAVIEW (Kitware, Inc., Clifton Park, NY). The following quantitative indices of flow morphology

were obtained: flow asymmetry ($Flow_{asymmetry}$), flow dispersion ($Flow_{dispersion}$), and helical flow index (HFI).

Flow asymmetry: Flow asymmetry ($Flow_{asymmetry}$) on each plane was obtained to assess whether flow was central or eccentric [47]. $Flow_{asymmetry}$ was obtained by calculating the centroid of the top 15% of peak systolic velocities ($V_{max}^{15\%}$) (point $\bar{x}_b = (x_b, y_b, z_b)$, Fig. 3), and measuring its distance to the geometric centroid of each aortic plane (point $\bar{x}_a = (x_a, y_a, z_a)$). The distance between centroids ($\|\bar{x}_b - \bar{x}_a\|$) is then divided by the equivalent radius of the plane (R_{eq})

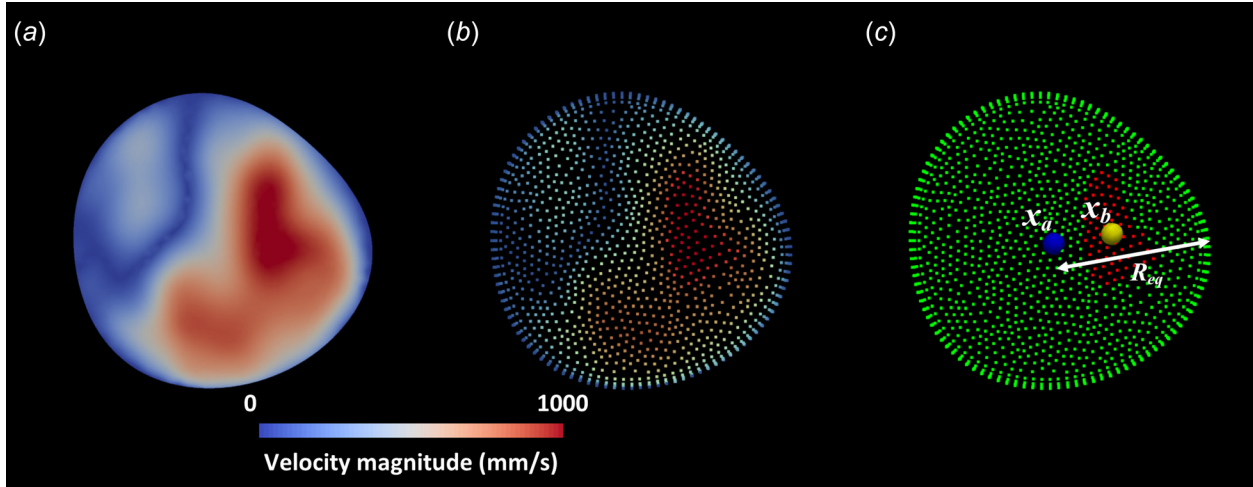


Fig. 3 (a) 2D representation of the velocity magnitude during peak systole, (b) velocity magnitude represented by individual dots for each nodal point of the aortic inflow computational mesh, and (c) red dots represent the top 15% of velocities at peak systole ($V_{\max}^{15\%}$), \bar{x}_a represents the centroid of the inflow face, \bar{x}_b represents the centroid of $V_{\max}^{15\%}$, and R_{eq} represents the equivalent radius of the inflow face

$$\text{Flow}_{\text{asymmetry}} = 100 \times \frac{\sqrt{(x_b - x_a)^2 + (y_b - y_a)^2 + (z_b - z_a)^2}}{R_{eq}} \quad (1)$$

A $\text{Flow}_{\text{asymmetry}}$ of 0% means that flow is central to the axis of the vessel, and a $\text{Flow}_{\text{asymmetry}}$ of 100% means that flow is completely eccentric and biased toward the periphery of the lumen (see Fig. 3).

Flow dispersion: This metric ($\text{Flow}_{\text{dispersion}}$) represents whether the flow at each plane is peaked or broad. $\text{Flow}_{\text{dispersion}}$ was calculated by dividing the area of the top 15% of peak systolic velocities ($V_{\max}^{15\%}$) by the total area of the plane

$$\text{Flow}_{\text{dispersion}} = 100 \times \frac{\text{area of } V_{\max}^{15\%}}{\text{area of plane}} \quad (2)$$

A high value of $\text{Flow}_{\text{dispersion}}$ means that the flow profile is broad and wide, whereas a low value indicates a pointed, sharp velocity profile.

Helical flow index: Helicity is a metric that represents the extent to which corkscrew-like motion occurs, and is governed by velocity and vorticity [48]. The kinetic helicity density per unit volume is defined as

$$H_k = V \cdot (\nabla \times V) \quad (3)$$

where V is the blood velocity and $(\nabla \times V)$ the vorticity. A helical flow index was calculated to quantitatively measure the degree of flow helicity. We released sets of approximately 1750 immaterial particles at 50 equally spaced time instants throughout the cardiac cycle, created within a small spherical region in the root of the aorta. Particles were continuously released and tracked along the course of the thoracic aorta for 40 cycles using a time-step equal to $T/50$, where T was the cardiac period. Analyses were performed using only particles, which had left the domain through the descending aortic outlet by the time the 40 cycles were completed. This meant that the final analysis used approximately 700,000 particles in each case. HFI_j is the helical flow index for each pathline, calculated over a particle trajectory j

$$\text{HFI}_j = \frac{1}{N_j} \sum_i^{N_j} |\psi_i| \quad (4)$$

Here, i is the dimensionless normalized helicity, calculated as the cosine of the angle between velocity and vorticity vectors at each point of the pathline, computed at the i th time-step after the particle entered the domain. N_j is the number of time-steps for which the j th particle was present in the domain. Steady Poiseuille flow gives a value of $\psi_i = 0$, whereas $|\psi_i| = 1$ occurs when flow is purely helical [48–50]. $\text{HFI}_{\text{systole}}$ is the average HFI_j over all pathlines during the systolic phase, and $\text{HFI}_{\text{diastole}}$ is the average HFI_j over all pathlines during the diastolic phase. Specifically, the j th particle is present for N_j time steps, which we index by the set $S_j = \{1, 2, \dots, N_j\}$. This set can be partitioned as two subsets, $S_{j,\text{systole}}$ and $S_{j,\text{diastole}}$, such that $S_{j,\text{systole}} \cup S_{j,\text{diastole}} = S_j$, and $S_{j,\text{systole}} \cap S_{j,\text{diastole}} = \emptyset$, where the step index is placed in $S_{j,\text{systole}}$ or $S_{j,\text{diastole}}$ according to whether that step occurred during the systolic or diastolic phase of the cardiac cycle. For subject A, the cardiac period was 1.0 s, and the interval $[0, 0.340]$ within each cycle constituted systole; for subject B, the cardiac period was 0.85 s, and the interval $[0.0, 0.357]$ within each cycle constituted systole. All other time points constituted diastole. We then define

$$\text{HFI}_{j,\text{systole}} = \frac{1}{|S_{j,\text{systole}}|} \sum_{i \in S_{j,\text{systole}}} |\psi_i|$$

and

$$\text{HFI}_{j,\text{diastole}} = \frac{1}{|S_{j,\text{diastole}}|} \sum_{i \in S_{j,\text{diastole}}} |\psi_i|$$

Finally, with J defined to be the set of all particles, which left the domain through the descending aortic outlet during the 40 cardiac cycles simulated, we compute

$$\text{HFI}_{\text{systole}} = \frac{1}{|J|} \sum_{j \in J} \text{HFI}_{j,\text{systole}}$$

and

$$\text{HFI}_{\text{diastole}} = \frac{1}{|J|} \sum_{j \in J} \text{HFI}_{j,\text{diastole}}$$

As noted above, $|J| \approx 700,000$.

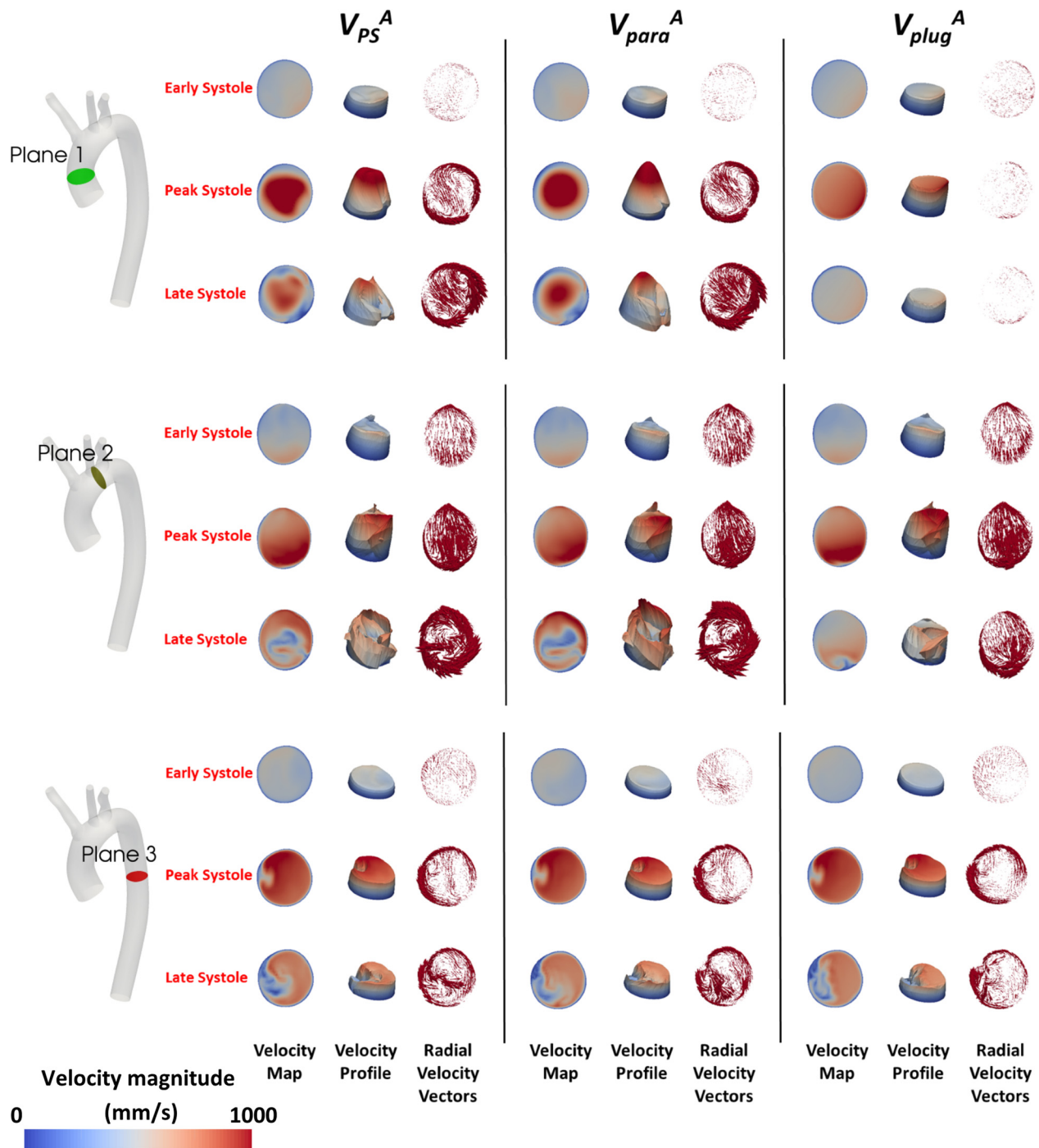


Fig. 4 2D and 3D representations of velocity magnitude, and radial (e.g., in-plane) velocity components at three planes of the thoracic aorta for subject A. Plane 1 corresponds to midascending aorta, plane 2 to transverse aortic arch, and plane 3 to mid-descending aorta.

3 Results

3.1 Velocity Patterns. Figure 2 shows the inflow velocity profiles for subjects A and B at peak systole. Despite having a slightly higher flow rate, subject A displays a profile (V_{PS}^A) with a lower velocity and broader pattern compared to subject B (V_{PS}^B). There is some similarity in both magnitude and 3D profile between V_{PS}^A and V_{para}^A ; however, V_{plug}^A is clearly different. Conversely, the high velocity and narrow eccentric profile of V_{PS}^B bear no resemblance to that of V_{para}^B or V_{plug}^B .

Figures 4 and 5 depict 2D and 3D visualizations of the velocity magnitude, and radial velocity vectors at three different aortic

locations (midascending, transverse arch, and midsending) at early, peak, and late systole for subjects A and B, respectively.

In the midascending aorta (plane 1) of subject A (healthy), the velocity maps and velocity profiles of V_{PS}^A and V_{para}^A are similar throughout the three phases of systole. The solution obtained with V_{plug}^A is, however, different for all time points except for early systole (Fig. 4). In the transverse aortic arch (plane 2), V_{PS}^A , V_{para}^A , and V_{plug}^A all show similar velocity maps and profiles for early and peak systole, but not for late systole. Finally, in the midsending aorta (plane 3), V_{PS}^A , V_{para}^A , and V_{plug}^A all show similar velocity maps throughout systole.

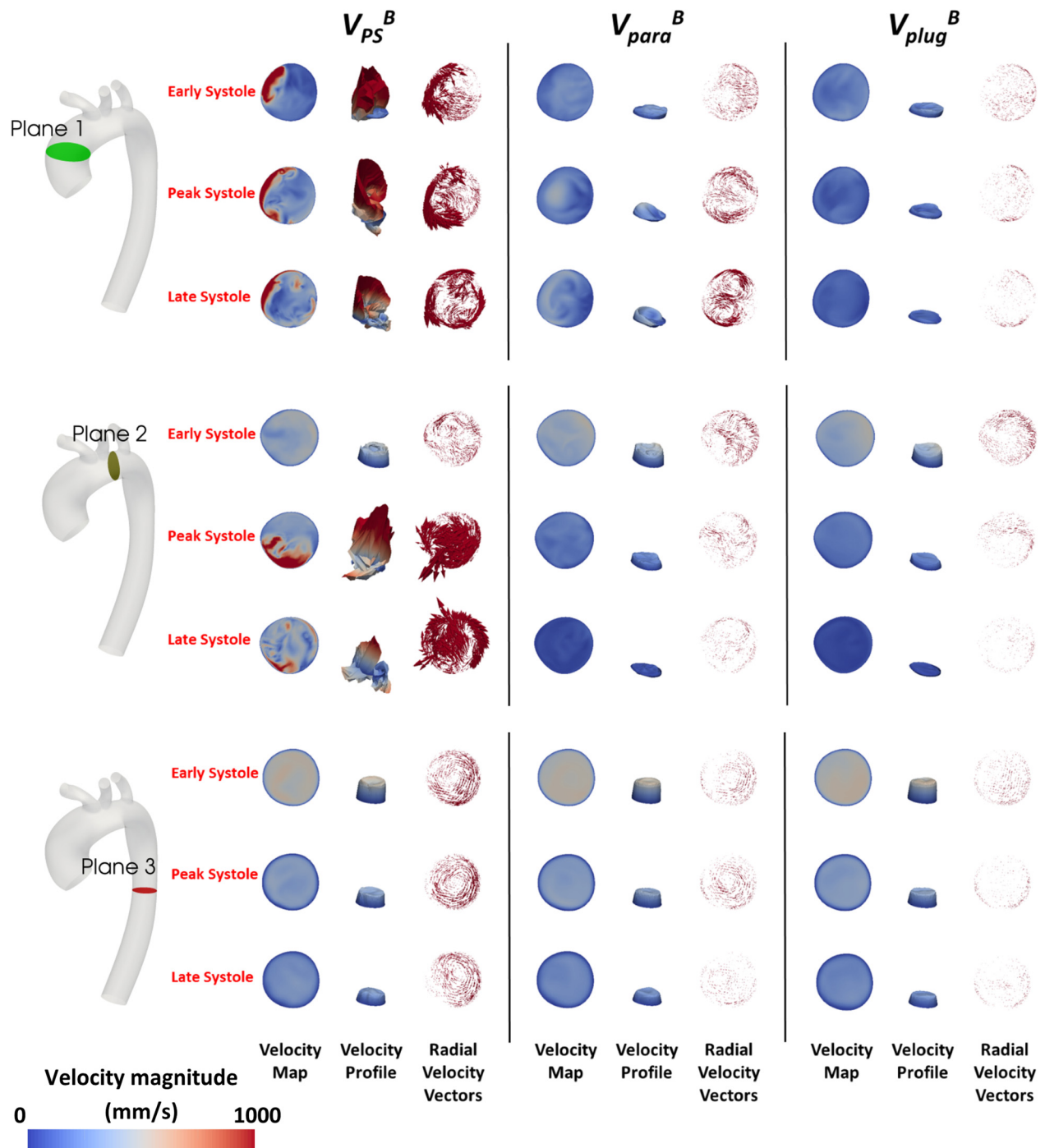


Fig. 5 2D and 3D representations of velocity magnitude, and radial (e.g., in-plane) velocity components at three planes of the thoracic aorta for subject B. Plane 1 corresponds to mid-ascending aorta, plane 2 to transverse aortic arch, and plane 3 to mid-descending aorta.

For subject B, the differences introduced by the different inflow velocity profiles (V_{PS}^B , V_{para}^B , V_{plug}^B) extend through most of the length of the thoracic aorta. Figure 5 reveals high velocity profiles in the patient-specific profile simulation (V_{PS}^B) in the ascending aorta (plane 1) at the lumen periphery (velocity map), and highly distorted and twisted flow (velocity profile). On the other hand, V_{para}^B and V_{plug}^B show a relatively even distribution of velocities over the cross section of the lumen. These differences are seen to continue along the transverse aortic arch (plane 2). As we go further to the descending aorta (plane 3), the velocity magnitude and

profile become virtually identical throughout the three phases of systole between V_{PS}^B , V_{para}^B , and V_{plug}^B .

Figures 4 and 5 also show the radial velocity vectors at the three aortic locations. Comparison of the vector direction and size is made for both subjects and for each inflow velocity profile. Figure 4 shows that V_{PS}^A and V_{para}^A show similar radial velocity vectors throughout all three planes of the thoracic aorta. V_{plug}^A shows very different profiles in peak and late systole in plane 1; however, these differences become smaller during early and peak systole in plane 2. By plane 3, all three simulations

show similar radial velocity vectors throughout the cardiac cycle.

Figure 5 shows that V_{PS}^B has large radial vectors circulating around the lumen in a helical fashion. These vectors are different in direction and size to the radial vectors obtained with V_{para}^B and V_{plug}^B , and remain so for all aortic locations.

3.2 Velocity Magnitude Waveforms. Figure 6 depicts waveforms for the maximum through-plane velocity (V_{max}), maximum radial velocity, and total flow for each of the three planes (midascending, transverse aortic arch, and middescending) for subjects A and B.

For subject A, despite having identical flow rates for the three simulations, V_{plug}^A clearly underestimates V_{max} in the midascending aorta and aortic arch compared to V_{PS}^A . Conversely, V_{para}^A slightly overestimates V_{max} in the ascending aorta and transverse aortic arch. The relative differences between radial velocities are much more apparent: V_{plug}^A clearly underestimates this component compared to V_{PS}^A and V_{para}^A , particularly in the ascending aorta. V_{para}^A overestimates radial velocities in plane 1 relative to V_{PS}^A , and produces similar radial velocity profiles in planes 2 and 3.

As for subject B, both V_{para}^B and V_{plug}^B grossly underestimate V_{max} when compared to V_{PS}^B in planes 1 and 2. By plane 3, V_{max} for V_{PS}^B declines and produces almost identical solutions as V_{para}^B and V_{plug}^B . This correlates with the development of similar through-plane velocity patterns and profiles among all three simulations in plane 3 (Fig. 5). As for the radial velocity profiles, V_{PS}^B shows significantly higher velocities compared to the idealized profiles throughout the aorta. This is consistent with the size of radial vectors seen in Fig. 5. It is interesting to note that in plane 3, despite all three simulations having almost identical through-plane V_{max} values, V_{PS}^B shows radial velocities twice as large compared to V_{para}^B and V_{plug}^B .

3.3 Helicity. Table 2 shows the values for HFI during systole and diastole. For subject A, HFI was significantly underestimated not only by V_{plug}^A but also (to a lesser degree) by V_{para}^A . For subject B, HFI was similar for all three simulations.

3.4 Velocity Pathlines. Figure 7 depicts three-dimensional immaterial particle pathlines and mean absolute HFI calculated using the subject-specific inflow velocity profile for the two subjects over a single cardiac cycle. Even though the numerical values of HFI in the subject-specific profile case are not substantially different between the healthy (subject A) and diseased (subject B) cases (see Table 2), the difference in particle trajectories is significant. In subject A, the particles have moved in a unidirectional manner down the aorta and by the end of the first cycle, they have almost left the domain. In contrast, particles injected in subject B are still in the ascending aorta after 900 ms, having followed a very tortuous path. The particles shown for subject B take almost twice as long as those shown for subject A to exit the simulation domain through the descending aortic boundary. Note that only eight particles are shown in this figure for the sake of clarity in the visualization. The HFI indices presented in Table 2 were calculated using a much larger number of pathlines (approximately 700,000).

3.5 Flow Asymmetry and Dispersion. V_{PS}^A and V_{PS}^B displayed very different $Flow_{asymmetry}$ trends throughout the aorta. V_{PS}^A showed symmetrical flow in plane 1, relatively asymmetrical flow in plane 2, and symmetrical flow in plane 3. Conversely, V_{PS}^B showed highly asymmetrical flow for most of the thoracic aorta (planes 1 and 2), with $Flow_{asymmetry} > 80\%$ (see Fig. 8). Interestingly, the idealized profiles V_{para} and V_{plug} for both subjects show similar trends in plane 1, 2, and 3 (Fig. 8).

Figure 9 shows the flow dispersion results for subjects A and B. $Flow_{dispersion}$ for V_{PS}^A was similar to the idealized profiles in planes

1 and 3. In the descending aorta (plane 3), flow became much broader for all three simulations. On the other hand, V_{PS}^B showed much smaller velocity dispersion compared to the two idealized profiles throughout the aorta.

4 Discussion

It is increasingly recognized that flow in the thoracic aorta contains significant radial (nonaxial) components associated with helical flow [51]. This is likely to be due to a combination of factors including ventricular twist and torsion during systole [52,53], the mechanics of the aortic valve and aortic root [54], and the curved morphology of the ascending, arch, and descending aorta [55–58]. From a physiological viewpoint, helical flow may comprise a degree of normal organ perfusion [59]. On the other hand, it has also been shown to play an important role in plaque deposition [60] and initiation of dissection [61]. Pritchard et al. [62] demonstrated differences in monocyte adhesion to the vascular wall (important cells in the pathogenesis of atherosclerotic plaques) related to the radial component of velocity. It is, therefore, imperative that CFD of the thoracic aorta can correctly mimic this helical flow in order to produce accurate simulations of blood flow.

In this paper, we presented a methodology for extracting velocity and flow data just distal to the aortic valve, segmenting, and mapping these data onto the inflow mesh of the CFD model. This approach, in combination with noninvasive pressure data and three-element Windkessel models for outflow boundary conditions, produced a patient-specific workflow for simulating thoracic aortic blood flow. Using this methodology, we have demonstrated the differences in aortic hemodynamics between simulations run with patient-specific inflow velocity profiles versus idealized inflow velocity profiles (e.g., parabolic and plug) on two different subjects, one healthy (subject A) and one presenting aortic valve disease (subject B). Subject B was chosen for this study because of the combination of aortic valve pathology and moderate aneurysm of the ascending aorta, a presentation frequently encountered by cardiothoracic surgeons and cardiologists.

A number of studies have been carried out on other parts of the vascular system, including the carotid arteries [26] and abdominal aorta [31,44], to examine the effects of different inflow boundary conditions on CFD simulations. The abdominal aorta has been investigated by Hardman et al. [48] who compared patient-specific inflow profiles to idealized Womersley profiles generated from the patient's flow-MRI center-line velocity data. They found that the idealized Womersley profile produced simplified flow patterns with an absence of helical flow. The helical flow index was lower in the Womersley simulation. They also found the maximum velocity of the idealized inlet simulation to be half the magnitude of the patient-specific simulations. The Womersley simulation also displayed smaller radial velocity vectors. These trends were similar to our findings in the thoracic aorta.

Morbiducci et al. investigated the effects of patient-specific inflow profiles versus idealized plug profiles in the thoracic aorta of a healthy subject, and found significant differences in hemodynamic results [37], in keeping with our study's results. They also compared the use of three-component versus single-component (through-plane) prescribed patient-specific inflow profiles, and found that single-component (through-plane) inflow profiles captured sufficient accuracy in hemodynamic results without the need for the use of three-component inflow profiles. This was also seen in the abdominal aorta by Chandra et al. [34], who compared three-component with single-component (through-plane) patient-specific inflow profiles in diseased abdominal aneurysms. In our study, we used single-component (through-plane) patient-specific inflow profiles, and assessed hemodynamics in both a healthy and a diseased subject. We further assessed other parameters such as $Flow_{asymmetry}$ and $Flow_{dispersion}$. Future work would benefit from investigating whether three-component patient-specific inflow

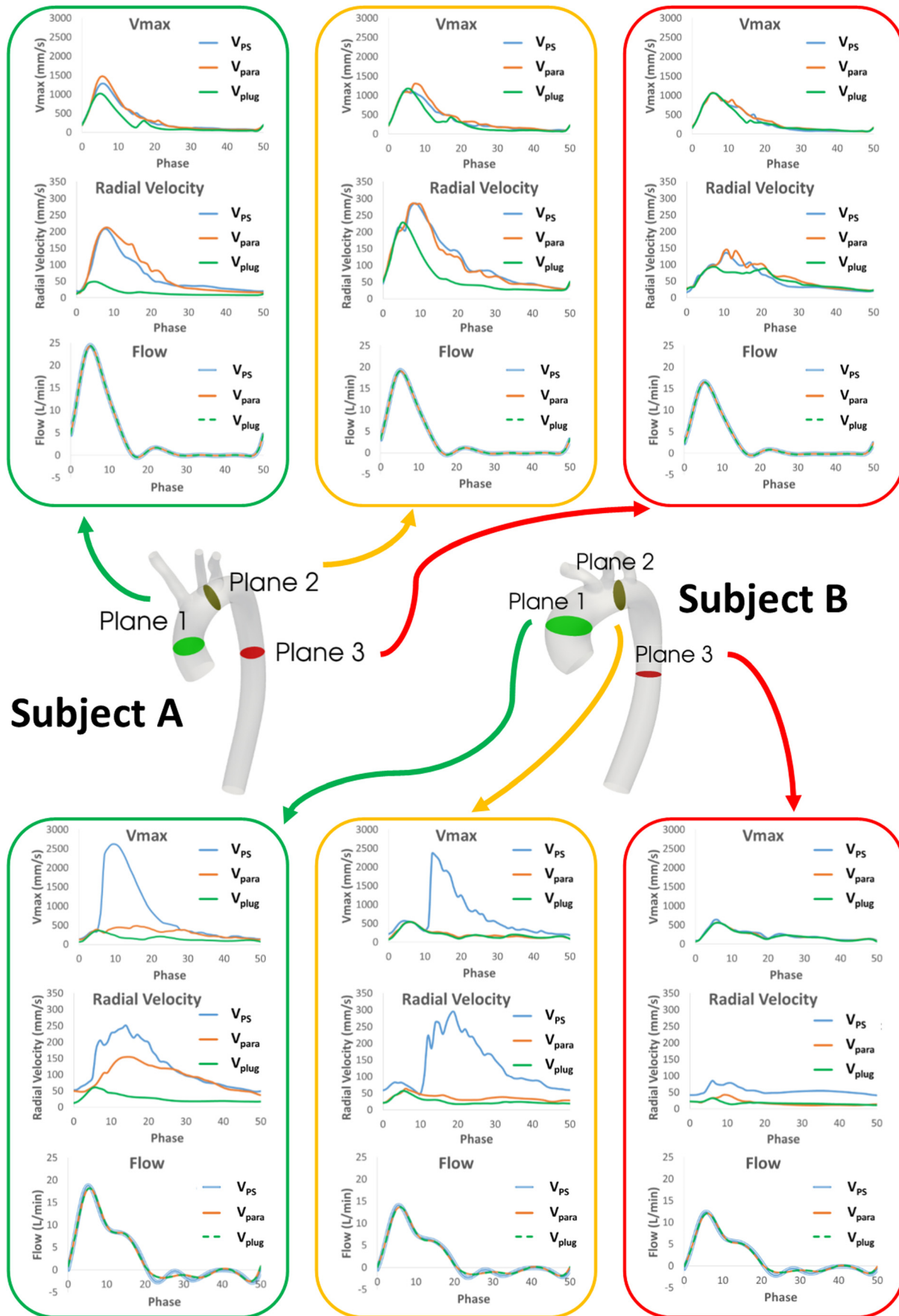


Fig. 6 Maximal through-plane velocity (V_{max}), radial (in-plane) velocity and flow rate along the cardiac cycle at three planes for subjects A and B

Table 2 Helical flow index during systole, diastole, and the whole cardiac cycle for the thoracic aorta for particles which traversed the aorta and left the simulation domain through the descending aortic boundary

	V_{PS}^A	V_{para}^A	V_{plug}^A	V_{PS}^B	V_{para}^B	V_{plug}^B
HFI ^{systole}	0.49	0.44	0.37	0.48	0.48	0.48
HFI ^{diastole}	0.49	0.44	0.37	0.50	0.51	0.51
HFI ^{cycle}	0.49	0.44	0.37	0.49	0.49	0.50

profiles yield different results in diseased states of the thoracic aorta.

Previous methods of mapping inflow velocity data to the model inlet have included the Schwarz–Christoffel method [34,63]. This method requires that the inlet is defined by a closed polygon, which normally is the case with polygonal meshes; however, there may be a restriction in other types of models. Particularly, relieving this polygonal constraint is useful when image data are segmented, as smooth closed curves are normally used for inlet delineation. In this study, our mapping scheme allows mapping of

the segmented image to any smooth rigid or nonrigid contour. It uses a flexible B-spline framework to map the inflow velocity data to the model inlet, and addresses changes in shape and size between the imaging data and the model inlet.

Our study demonstrated important differences between healthy and diseased aortic hemodynamics, and also stark differences for each subject between simulations run with patient-specific versus idealized inflow velocity profiles.

In the case of the healthy aortic valve (subject A), the idealized parabolic profile V_{para}^A produced velocity maps and profiles similar to those obtained with the patient-specific profile V_{PS}^A . Furthermore, other parameters such as V_{max} and radial velocity were also comparable between V_{PS}^A and V_{para}^A . This indicates that a parabolic profile is a reasonable choice if an idealized inflow profile is to be used due to the lack of patient-specific velocity data for simulations involving disease-free aortic valves. However, it must be noted that despite the similarities mentioned previously, other hemodynamic parameters showed significant differences between simulations run with idealized and patient-specific velocity profiles. For example, $Flow_{asymmetry}$ in the transverse aortic arch was almost double in V_{para}^A compared to V_{PS}^A . Helicity was also significantly underestimated during systole and diastole using the

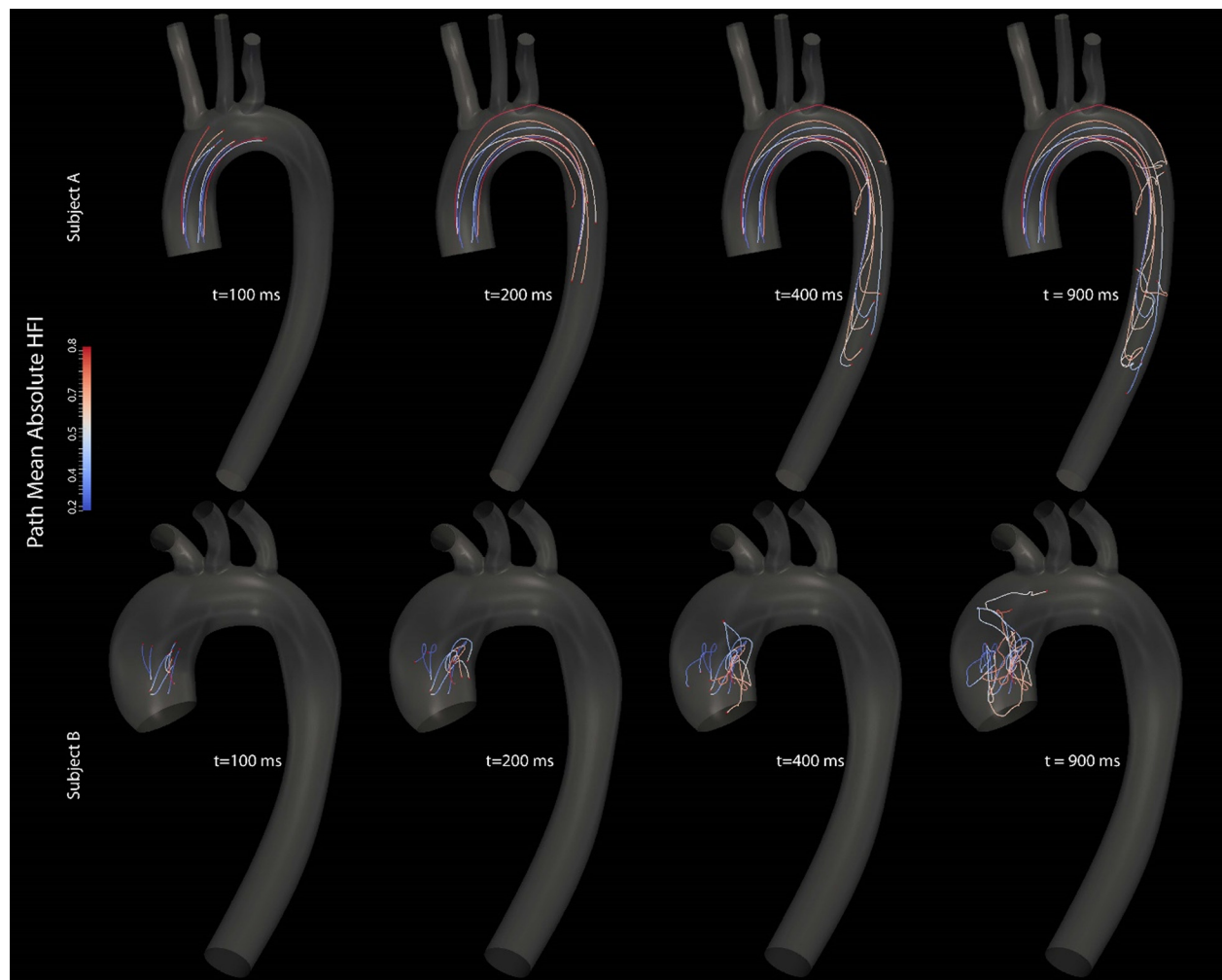


Fig. 7 Pathlines and mean absolute HFI calculated using the subject-specific inflow velocity profile for subject A (top) and subject B (bottom) at $t = 100, 200, 400,$ and 900 ms. Even though the numerical values of HFI are not substantially different between the healthy (subject A) and diseased (subject B) cases (see Table 2), the difference in particle trajectories is remarkable. In subject A, the particles have moved in a unidirectional manner down the aorta and by the end of the first cycle, they have almost left the domain. In contrast, particles injected in subject B are still in the ascending aorta after 900 ms, having followed a very tortuous path. Note: only a small number of particles are tracked for the sake of clarity in the visualization. The HFI indices were calculated using a much larger number of pathlines (approximately 700,000).

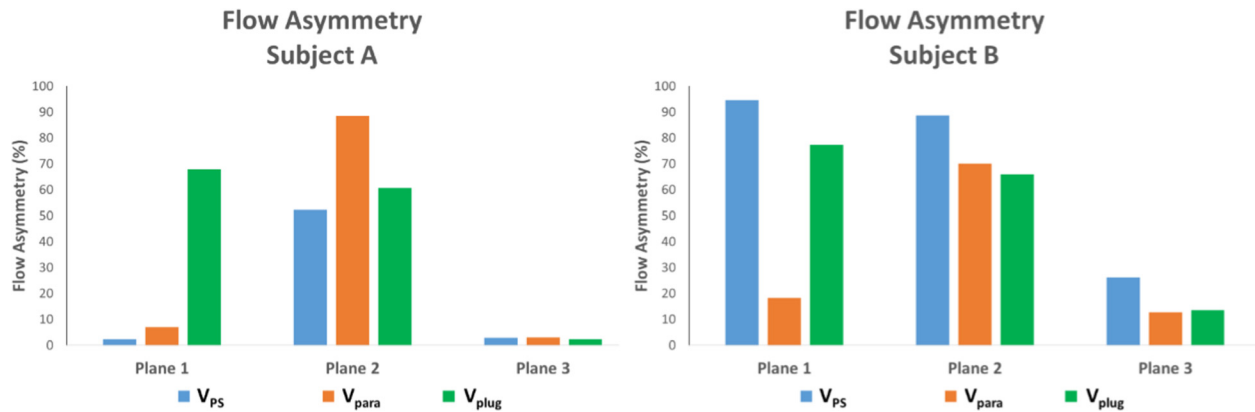


Fig. 8 Flow_{asymmetry} along three planes of the thoracic aorta for subjects A and B

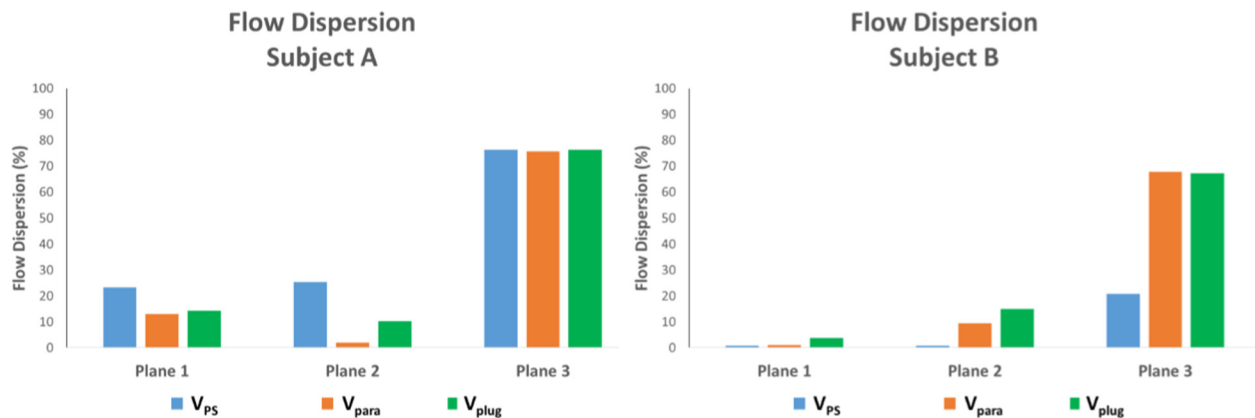


Fig. 9 Flow_{dispersion} along three planes of the thoracic aorta for subjects A and B

idealized velocity profiles. Furthermore, solutions obtained with the idealized plug profile V_{plug}^A differed quite substantially from the patient-specific profile V_{ps}^A in the ascending aorta.

In the case of the subject with aortic valvular stenosis (subject B), simulations run with the patient-specific velocity profile V_{ps}^B revealed how the eccentric asymmetrical inflow profile led to highly complex velocity maps and velocity profiles along most of the length of the thoracic aorta. These complex velocity patterns were not replicated by the two idealized velocity profiles. Despite having identical flow rates to V_{ps}^B , the idealized inflow profiles produced different peak velocities (V_{max}) and velocity patterns. Results obtained with idealized inflow profiles V_{para}^B and V_{plug}^B did not demonstrate the high degree of radial velocity obtained with V_{ps}^B , neither in direction nor in magnitude.

The results acquired for HFI (Table 2) showed relatively similar values for the patient-specific simulations of both the healthy (subject A) and diseased subjects (subject B). However, based on the particle pathlines seen in Fig. 7 (which were used to calculate helicity), the trajectories for these two subjects are significantly different. This may question the lack of suitability of HFI as a hemodynamic parameter in capturing relevant numerical differences between healthy and diseased patient-specific velocity profiles.

Our results in the BAV subject are in keeping with four-dimensional flow MRI studies by Mahadevia et al. [47], where flow exiting the bicuspid valve was found to be eccentric and asymmetrical. Their 3D streamlines showed high velocity jets and flow impingement in the greater curvature of the ascending aorta,

similar to our streamline results for V_{ps}^B . Other studies by Barker et al. [64] showed the effect of bicuspid valves in causing increasing shear stresses in the ascending aorta. These findings lend further support to the use of accurate patient-specific inflow profiles in assessing diseased aortic hemodynamics. Most differences observed between patient-specific and idealized simulations spanned the entire ascending aorta and aortic arch, and started to dissipate in the descending aorta. Here, velocity maps and profiles, radial vectors, V_{max} , and Flow_{asymmetry} equaled out to form similar patterns and magnitudes. The descending thoracic aorta is the first relatively straight location of the thoracic aorta. If free of disease, its cross section remains relatively constant. These properties allow the flow to reattach and become fully developed. Our results provide insight into the factors governing hemodynamics in different parts of the thoracic aorta. The most striking differences in hemodynamic parameters between the patient-specific and idealized simulations were seen in the ascending aorta (plane 1). This shows that ascending aorta hemodynamics is largely dependent on the inflow, which is itself dependent on aortic valve morphology. Indeed, there is evidence that bicuspid aortic valve is often associated with aneurysms of the ascending aorta [65]. It remains to be elucidated whether this is primarily caused by genetic factors [66] or altered hemodynamics. Our results also show that descending aortic hemodynamics are independent of inflow velocity profile, indicating that disease of the descending aorta is not related to aortic valve pathology.

This study demonstrates that the use of idealized inflow velocity profiles produces hemodynamic solutions in which differences

between diseased and healthy subjects are minimized, therefore making them highly unsuitable for disease research.

4.1 Limitations. In our model, we assumed the vessels to behave in a rigid manner. However, the flow-MRI information was dynamically acquired on a fixed Eulerian plane, containing different material sections of the ascending aorta due to its complex motion and deformation. Indeed, the aortic root moves up and down following the contraction and relaxation of the heart, and also deforms radially due to the pulsatile pressure. Our method mapped the history of velocities enclosed within the dynamic segmentations of the aortic root on the fixed Eulerian plane onto the fixed inlet face of the rigid aortic model reconstructed from single-phase MRA data. This transformation alters the true inflow velocity profile of the subject. To address this issue, a flow-MRI sequence that measures velocity on a Lagrangian plane moving together with the aorta is needed. Furthermore, a fluid–structure interaction (FSI) simulation that can accommodate the large displacements and deformations of the ascending thoracic aorta is also necessary. This can be accomplished with an arbitrary Lagrangian–Eulerian formulation [67], although this approach will significantly increase the computational cost. As to how much a full FSI model would alter the results seen in this study remains to be investigated. However, Brown et al. compared a full FSI model with that of a rigid model in a healthy aorta, and found similar results in flow fields, including very similar HFI results [68]. Future work to assess the impact of FSI models in simulations of diseased aortas would be important.

Another limitation of the present work is the lack of information on flow splits between the different outflow branches of the aorta. Due to this lack of data, we distributed the measured aortic inflow according to the cross-sectional area of the different branches. This approximation might be inaccurate, especially in disease situations, and therefore it may alter the flow patterns in the aorta. Additional flow-MRI measurements in the upper branch vessels and descending aorta would remedy this problem without increasing significantly the total scanning time.

Finally, the hemodynamics presented in this paper corresponds to two different but illustrative cases. However, all data and measurements used in the CFD models pertained to these patients, and our simulations were therefore patient-specific. Our study concentrates on velocity patterns, through-plane and radial velocity, helicity, flow asymmetry, and dispersion. Another important hemodynamic force not analyzed in this study is wall shear stress, which plays a significant role in vasculopathy and mechanobiological responses in the vessel wall. Analysis of WSS to any depth would form the basis for a separate manuscript. We have shown in another study that WSS in the ascending aorta is significantly affected by various morphologies of the aortic valve, which have an individual effect on the inflow boundary conditions [69].

5 Conclusion

We have presented a comparative study using patient-specific velocity inflow boundary conditions versus idealized velocity boundary conditions based on MRI measurements of velocity and flow in the ascending aorta. We have extracted patient-specific through-plane blood velocity data from flow-MRI and applied them as inflow boundary conditions to assess the effects of patient-specific inflow profiles versus idealized inflow profiles on hemodynamics in the thoracic aorta. Furthermore, we have also evaluated indices of flow disturbance such as helicity based on the computation of pathlines. Our analysis revealed that idealized inflow boundary conditions can significantly alter velocity patterns and underestimate velocity magnitudes, radial velocity components, helicity, and complex flow in the thoracic aorta. The aortic valve and its highly complex structure and predisposition to pathological change means that the inflow

velocities into the thoracic aorta can be highly variable. This study demonstrated the importance of utilizing patient-specific boundary conditions to produce meaningful results not only in healthy but also in diseased aortic hemodynamics.

Acknowledgment

The authors wish to acknowledge Simmetrix, Inc.² for their MeshSim mesh generation library and Dr. Desmond Dillon-Murphy for his expertise and technical assistance.

Funding Data

- British Heart Foundation (Grant No. NH/11/5/29058).
- European Research Council (Grant Agreement No. 307532).
- Royal College of Surgeons of England (Research Fellowship).

Nomenclature

CFD = computational fluid dynamics
HFI = helical flow index
MRI = magnetic resonance imaging
MRA = magnetic resonance angiography

References

- [1] Friedman, M. H., Hutchins, G. M., Barger, C. B., Deters, O. J., and Mark, F. F., 1981, "Correlation Between Intimal Thickness and Fluid Shear in Human Arteries," *Atherosclerosis*, **39**(3), pp. 425–436.
- [2] Zarins, C. K., Giddens, D. P., Bharadvaj, B. K., Sottiurai, V. S., Mabon, R. F., and Glagov, S., 1983, "Carotid Bifurcation Atherosclerosis. Quantitative Correlation of Plaque Localization With Flow Velocity Profiles and Wall Shear Stress," *Circ. Res.*, **53**(4), pp. 502–514.
- [3] Yeung, J. J., Kim, H. J., Abbruzzese, T. A., Vignon-Clementel, I. E., Draney-Blomme, M. T., Yeung, K. K., Perkas, I., Herfkens, R. J., Taylor, C. A., and Dalman, R. L., 2006, "Aortoiliac Hemodynamic and Morphologic Adaptation to Chronic Spinal Cord Injury," *J. Vasc. Surg.*, **44**(6), pp. 1254–1265.
- [4] Humphrey, J. D., and Taylor, C. A., 2008, "Intracranial and Abdominal Aortic Aneurysms: Similarities, Differences, and Need for a New Class of Computational Models," *Annu. Rev. Biomed. Eng.*, **10**(1), pp. 221–246.
- [5] Chien, S., Li, S., and Shyy, Y. J., 1998, "Effects of Mechanical Forces on Signal Transduction and Gene Expression in Endothelial Cells," *Hypertension*, **31**(1), pp. 162–169.
- [6] Davies, P. F., 1995, "Flow-Mediated Endothelial Mechanotransduction," *Physiol. Rev.*, **75**(3), pp. 519–560.
- [7] Gibbons, G. H., and Dzau, V. J., 1994, "The Emerging Concept of Vascular Remodeling," *N. Engl. J. Med.*, **330**(20), pp. 1431–1438.
- [8] Langille, B. L., 1996, "Arterial Remodeling: Relation to Hemodynamics," *Can. J. Physiol. Pharmacol.*, **74**(7), pp. 834–841.
- [9] Humphrey, J. D., 2008, "Mechanisms of Arterial Remodeling in Hypertension: Coupled Roles of Wall Shear and Intramural Stress," *Hypertension*, **52**(2), pp. 195–200.
- [10] Xiong, G., Figueroa, C. A., Xiao, N., and Taylor, C. A., 2011, "Simulation of Blood Flow in Deformable Vessels Using Subject-Specific Geometry and Spatially Varying Wall Properties," *Int. J. Numer. Method Biomed. Eng.*, **27**(7), pp. 1000–1016.
- [11] Milner, J. S., Moore, J. A., Rutt, B. K., and Steinman, D. A., 1998, "Hemodynamics of Human Carotid Artery Bifurcations: Computational Studies With Models Reconstructed From Magnetic Resonance Imaging of Normal Subjects," *J. Vasc. Surg.*, **28**(1), pp. 143–156.
- [12] Cebal, J. R., Yim, P. J., Lohner, R., Soto, O., and Choyke, P. L., 2002, "Blood Flow Modeling in Carotid Arteries With Computational Fluid Dynamics and MR Imaging," *Acad. Radiol.*, **9**(11), pp. 1286–1299.
- [13] Fillingim, M. F., Raghavan, M. L., Marra, S. P., Cronenwett, J. L., and Kennedy, F. E., 2002, "In Vivo Analysis of Mechanical Wall Stress and Abdominal Aortic Aneurysm Rupture Risk," *J. Vasc. Surg.*, **36**(3), pp. 589–597.
- [14] Fillingim, M. F., Marra, S. P., Raghavan, M. L., and Kennedy, F. E., 2003, "Prediction of Rupture Risk in Abdominal Aortic Aneurysm During Observation: Wall Stress Versus Diameter," *J. Vasc. Surg.*, **37**(4), pp. 724–732.
- [15] Les, A. S., Shadden, S. C., Figueroa, C. A., Park, J. M., Tedesco, M. M., Herfkens, R. J., Dalman, R. L., and Taylor, C. A., 2010, "Quantification of Hemodynamics in Abdominal Aortic Aneurysms During Rest and Exercise Using Magnetic Resonance Imaging and Computational Fluid Dynamics," *Ann. Biomed. Eng.*, **38**(4), pp. 1288–1313.

²<http://www.simmetrix.com/>

- [16] Li, Z., and Kleinstreuer, C., 2005, "Blood Flow and Structure Interactions in a Stented Abdominal Aortic Aneurysm Model," *Med. Eng. Phys.*, **27**(5), pp. 369–382.
- [17] Stuhne, G. R., and Steinman, D. A., 2004, "Finite-Element Modeling of the Hemodynamics of Stented Aneurysms," *ASME J. Biomech. Eng.*, **126**(3), pp. 382–387.
- [18] Migliavacca, F., Balossino, R., Pennati, G., Dubini, G., Hsia, T. Y., de Leval, M. R., and Bove, E. L., 2006, "Multiscale Modelling in Biofluidynamics: Application to Reconstructive Paediatric Cardiac Surgery," *J. Biomech.*, **39**(6), pp. 1010–1020.
- [19] Soerensen, D. D., Pekkan, K., de Zelicourt, D., Sharma, S., Kanter, K., Fogel, M., and Yoganathan, A. P., 2007, "Introduction of a New Optimized Total Cavopulmonary Connection," *Ann. Thorac. Surg.*, **83**(6), pp. 2182–2190.
- [20] Taylor, C. A., Draney, M. T., Ku, J. P., Parker, D., Steele, B. N., Wang, K., and Zarins, C. K., 1999, "Predictive Medicine: Computational Techniques in Therapeutic Decision-Making," *Comput. Aided Surg.*, **4**(5), pp. 231–247.
- [21] Lee, S. W., and Steinman, D. A., 2007, "On the Relative Importance of Rheology for Image-Based CFD Models of the Carotid Bifurcation," *ASME J. Biomech. Eng.*, **129**(2), pp. 273–278.
- [22] Lee, K. W., Wood, N. B., and Xu, X. Y., 2004, "Ultrasound Image-Based Computer Model of a Common Carotid Artery With a Plaque," *Med. Eng. Phys.*, **26**(10), pp. 823–840.
- [23] Steinman, D. A., 2002, "Image-Based Computational Fluid Dynamics Modeling in Realistic Arterial Geometries," *Ann. Biomed. Eng.*, **30**(4), pp. 483–497.
- [24] Wake, A. K., Oshinski, J. N., Tannenbaum, A. R., and Giddens, D. P., 2009, "Choice of In Vivo Versus Idealized Velocity Boundary Conditions Influences Physiologically Relevant Flow Patterns in a Subject-Specific Simulation of Flow in the Human Carotid Bifurcation," *ASME J. Biomech. Eng.*, **131**(2), p. 021013.
- [25] Moyle, K. R., Antiga, L., and Steinman, D. A., 2006, "Inlet Conditions for Image-Based CFD Models of the Carotid Bifurcation: Is It Reasonable to Assume Fully Developed Flow?," *ASME J. Biomech. Eng.*, **128**(3), pp. 371–379.
- [26] Steinman, D. A., Thomas, J. B., Ladak, H. M., Milner, J. S., Rutt, B. K., and Spence, J. D., 2002, "Reconstruction of Carotid Bifurcation Hemodynamics and Wall Thickness Using Computational Fluid Dynamics and MRI," *Magn. Reson. Med.*, **47**(1), pp. 149–159.
- [27] Vignon-Clementel, I. E., Alberto Figueroa, C., Jansen, K. E., and Taylor, C. A., 2006, "Outflow Boundary Conditions for Three-Dimensional Finite Element Modeling of Blood Flow and Pressure in Arteries," *Comput. Methods Appl. Mech. Eng.*, **195**(29–32), pp. 3776–3796.
- [28] Campbell, I. C., Ries, J., Dhawan, S. S., Quyyumi, A. A., Taylor, W. R., and Oshinski, J. N., 2012, "Effect of Inlet Velocity Profiles on Patient-Specific Computational Fluid Dynamics Simulations of the Carotid Bifurcation," *ASME J. Biomech. Eng.*, **134**(5), p. 051001.
- [29] Sigovan, M., Dwyerfeldt, P., Wrenn, J., Tseng, E. E., Saloner, D., and Hope, M. D., 2015, "Extended 3D Approach for Quantification of Abnormal Ascending Aortic Flow," *Magn. Reson. Imaging*, **33**(5), pp. 695–700.
- [30] Waller, B. F., Howard, J., and Fess, S., 1994, "Pathology of Aortic Valve Stenosis and Pure Aortic Regurgitation: A Clinical Morphologic Assessment—Part II," *Clin. Cardiol.*, **17**(3), pp. 150–156.
- [31] Waller, B., Howard, J., and Fess, S., 1994, "Pathology of Aortic Valve Stenosis and Pure Aortic Regurgitation: A Clinical Morphologic Assessment—Part I," *Clin. Cardiol.*, **17**(2), pp. 85–92.
- [32] Hoffman, J. I., and Kaplan, S., 2002, "The Incidence of Congenital Heart Disease," *J. Am. Coll. Cardiol.*, **39**(12), pp. 1890–1900.
- [33] Della Corte, A., Bancone, C., Quarto, C., Dialeto, G., Covino, F. E., Scardone, M., Caianiello, G., and Cotrufo, M., 2007, "Predictors of Ascending Aortic Dilatation With Bicuspid Aortic Valve: A Wide Spectrum of Disease Expression," *Eur. J. Cardiothorac. Surg.*, **31**(3), pp. 397–404.
- [34] Chandra, S., Raut, S. S., Jana, A., Biederman, R. W., Doyle, M., Muluk, S. C., and Finol, E. A., 2013, "Fluid-Structure Interaction Modeling of Abdominal Aortic Aneurysms: The Impact of Patient-Specific Inflow Conditions and Fluid/Solid Coupling," *ASME J. Biomech. Eng.*, **135**(8), p. 081001.
- [35] Marzo, A., Singh, P., Reymond, P., Stergiopoulos, N., Patel, U., and Hose, R., 2009, "Influence of Inlet Boundary Conditions on the Local Haemodynamics of Intracranial Aneurysms," *Comput. Methods Biomech. Biomed. Eng.*, **12**(4), pp. 431–444.
- [36] Myers, J. G., Moore, J. A., Ojha, M., Johnston, K. W., and Ethier, C. R., 2001, "Factors Influencing Blood Flow Patterns in the Human Right Coronary Artery," *Ann. Biomed. Eng.*, **29**(2), pp. 109–120.
- [37] Morbiducci, U., Ponzini, R., Gallo, D., Bignardi, C., and Rizzo, G., 2013, "Inflow Boundary Conditions for Image-Based Computational Hemodynamics: Impact of Idealized Versus Measured Velocity Profiles in the Human Aorta," *J. Biomech.*, **46**(1), pp. 102–109.
- [38] Efsthathopoulos, E. P., Pataoukas, G., Pantos, I., Benekos, O., Katritsis, D., and Kelekis, N. L., 2008, "Wall Shear Stress Calculation in Ascending Aorta Using Phase Contrast Magnetic Resonance Imaging. Investigating Effective Ways to Calculate It in Clinical Practice," *Phys. Med.*, **24**(4), pp. 175–181.
- [39] Mynard, J. P., Wasserman, B. A., and Steinman, D. A., 2013, "Errors in the Estimation of Wall Shear Stress by Maximum Doppler Velocity," *Atherosclerosis*, **227**(2), pp. 259–266.
- [40] Figueroa, C., Khlebnikov, R., Lau, K. D., Arthurs, C. J., Dillon-Murphy, D., Alastruey-Armon, J., and Aguirre, M., 2017, "Crimson," Crimson, Austin, TX, accessed Sept. 30, 2017, www.crimson.software
- [41] Wang, K. C., Dutton, R. W., and Taylor, C. A., 1999, "Improving Geometric Model Construction for Blood Flow Modeling," *IEEE Eng. Med. Biol. Mag.*, **18**(6), pp. 33–39.
- [42] Muller, J., Sahni, O., Li, X., Jansen, K. E., Shephard, M. S., and Taylor, C. A., 2005, "Anisotropic Adaptive Finite Element Method for Modelling Blood Flow," *Comput. Methods Biomech. Biomed. Eng.*, **8**(5), pp. 295–305.
- [43] Whiting, C., and Jansen, K., 2001, "A Stabilized Finite Element Method for the Incompressible Navier–Stokes Equations Using a Hierarchical Basis," *Int. J. Numer. Methods Fluids*, **35**(1), pp. 93–116.
- [44] Figueroa, C. A., Vignon-Clementel, I. E., Jansen, K. C., Hughes, T. J., and Taylor, C. A., 2006, "A Coupled Momentum Method for Modeling Blood Flow in Three-Dimensional Deformable Arteries," *Comput. Methods Appl. Mech. Eng.*, **195**(41–43), pp. 5685–5706.
- [45] Vignon-Clementel, I. E., Figueroa, C. A., Jansen, K. E., and Taylor, C. A., 2010, "Outflow Boundary Conditions for 3D Simulations of Non-Periodic Blood Flow and Pressure Fields in Deformable Arteries," *Comput. Methods Biomech. Biomed. Eng.*, **13**(5), pp. 625–640.
- [46] Xiao, N., Alastruey, J., and Figueroa, C. A., 2014, "A Systematic Comparison Between 1-D and 3-D Hemodynamics in Compliant Arterial Models," *Int. J. Numer. Method Biomed. Eng.*, **30**(2), pp. 204–231.
- [47] Mahadevia, R., Barker, A. J., Schnell, S., Entezari, P., Kansal, P., Fedak, P. W., Malaisrie, S. C., McCarthy, P., Collins, J., Carr, J., and Markl, M., 2014, "Bicuspid Aortic Cusp Fusion Morphology Alters Aortic Three-Dimensional Outflow Patterns, Wall Shear Stress, and Expression of Aortopathy," *Circulation*, **129**(6), pp. 673–682.
- [48] Hardman, D., Semple, S. I., Richards, J. M., and Hoskins, P. R., 2013, "Comparison of Patient-Specific Inlet Boundary Conditions in the Numerical Modelling of Blood Flow in Abdominal Aortic Aneurysm Disease," *Int. J. Numer. Method Biomed. Eng.*, **29**(2), pp. 165–178.
- [49] Morbiducci, U., Ponzini, R., Rizzo, G., Cadioli, M., Esposito, A., De Cobelli, F., Del Maschio, A., Montevercchi, F. M., and Redaelli, A., 2009, "In Vivo Quantification of Helical Blood Flow in Human Aorta by Time-Resolved Three-Dimensional Cine Phase Contrast Magnetic Resonance Imaging," *Ann. Biomed. Eng.*, **37**(3), pp. 516–531.
- [50] Grigioni, M., Daniele, C., Morbiducci, U., Del Gaudio, C., D'Avenio, G., Balducci, A., and Barbaro, V., 2005, "A Mathematical Description of Blood Spiral Flow in Vessels: Application to a Numerical Study of Flow in Arterial Bending," *J. Biomech.*, **38**(7), pp. 1375–1386.
- [51] Markl, M., Draney, M. T., Hope, M. D., Levin, J. M., Chan, F. P., Alley, M. T., Pelc, N. J., and Herfkens, R. J., 2004, "Time-Resolved 3-Dimensional Velocity Mapping in the Thoracic Aorta: Visualization of 3-Directional Blood Flow Patterns in Healthy Volunteers and Patients," *J. Comput. Assisted Tomogr.*, **28**(4), pp. 459–468.
- [52] Baciewicz, F. A., Penney, D. G., Marinelli, W. A., and Marinelli, R., 1991, "Torsional Ventricular Motion and Rotary Blood Flow. What is the Clinical Significance," *Cardiac Chronicle*, **5**, pp. 1–8.
- [53] Farthing, S., and Peronneau, P., 1979, "Flow in the Thoracic Aorta," *Cardiovasc. Res.*, **13**(11), pp. 607–620.
- [54] Bellhouse, B. J., and Reid, K. G., 1969, "Fluid Mechanics of the Aortic Valve," *Br. Heart J.*, **31**(3), p. 391.
- [55] Chandran, K. B., 1993, "Flow Dynamics in the Human Aorta," *ASME J. Biomech. Eng.*, **115**(4B), pp. 611–616.
- [56] Chandran, K. B., Yearwood, T. L., and Wieting, D. W., 1979, "An Experimental Study of Pulsatile Flow in a Curved Tube," *J. Biomech.*, **12**(10), pp. 793–805.
- [57] Yearwood, T. L., and Chandran, K. B., 1980, "Experimental Investigation of Steady Flow Through a Model of the Human Aortic Arch," *J. Biomech.*, **13**(12), pp. 1075–1088.
- [58] Yearwood, T. L., and Chandran, K. B., 1982, "Physiological Pulsatile Flow Experiments in a Model of the Human Aortic Arch," *J. Biomech.*, **15**(9), pp. 683–704.
- [59] Frazin, L. J., Vonesh, M. J., Chandran, K. B., Shipkowitz, T., Yaacoub, A. S., and McPherson, D. D., 1996, "Confirmation and Initial Documentation of Thoracic and Abdominal Aortic Helical Flow. An Ultrasound Study," *ASAIO J.*, **42**(6), pp. 951–956.
- [60] Kilner, P. J., Yang, G. Z., Mohiaddin, R. H., Firmin, D. N., and Longmore, D. B., 1993, "Helical and Retrograde Secondary Flow Patterns in the Aortic Arch Studied by Three-Directional Magnetic Resonance Velocity Mapping," *Circulation*, **88**(5), pp. 2235–2247.
- [61] Frazin, L. J., Lanza, G., Vonesh, M., Khasho, F., Spitzzeri, C., McGee, S., Mehlmann, D., Chandran, K. B., Talano, J., and McPherson, D., 1990, "Functional Chiral Asymmetry in Descending Thoracic Aorta," *Circulation*, **82**(6), pp. 1985–1994.
- [62] Pritchard, W. F., Davies, P. F., Derafshi, Z., Polacek, D. C., Tsao, R., Dull, R. O., Jones, S. A., and Giddens, D. P., 1995, "Effects of Wall Shear Stress and Fluid Recirculation on the Localization of Circulating Monocytes in a Three-Dimensional Flow Model," *J. Biomech.*, **28**(12), pp. 1459–1469.
- [63] Boutsianis, E., Gupta, S., Boomsma, K., and Poulikakos, D., 2008, "Boundary Conditions by Schwarz-Christoffel Mapping in Anatomically Accurate Hemodynamics," *Ann. Biomed. Eng.*, **36**(12), pp. 2068–2084.
- [64] Barker, A. J., Lanning, C., and Shandas, R., 2010, "Quantification of Hemodynamic Wall Shear Stress in Patients With Bicuspid Aortic Valve Using Phase-Contrast MRI," *Ann. Biomed. Eng.*, **38**(3), pp. 788–800.
- [65] Nistri, S., Sorbo, M. D., Marin, M., Palisi, M., Scognamiglio, R., and Thiene, G., 1999, "Aortic Root Dilatation in Young Men With Normally Functioning Bicuspid Aortic Valves," *Heart*, **82**(1), pp. 19–22.

- [66] Abdulkareem, N., Smelt, J., and Jahangiri, M., 2013, "Bicuspid Aortic Valve Aortopathy: Genetics, Pathophysiology and Medical Therapy," *Interact. Cardiovasc. Thorac. Surg.*, **17**(3), pp. 554–559.
- [67] Taylor, C. A., and Figueroa, C. A., 2009, "Patient-Specific Modeling of Cardiovascular Mechanics," *Annu. Rev. Biomed. Eng.*, **11**(1), pp. 109–134.
- [68] Brown, A. G., Shi, Y., Marzo, A., Staicu, C., Valverde, I., Beerbaum, P., Lawford, P. V., and Hose, D. R., 2012, "Accuracy vs. Computational Time: Translating Aortic Simulations to the Clinic," *J. Biomech.*, **45**(3), pp. 516–523.
- [69] Youssefi, P., Gomez, A., He, T., Anderson, L., Bunce, N., Sharma, R., Figueroa, C. A., and Jahangiri, M., 2017, "Patient-Specific Computational Fluid Dynamics-Assessment of Aortic Hemodynamics in a Spectrum of Aortic Valve Pathologies," *J. Thorac. Cardiovasc. Surg.*, **153**(1), pp. 8–20.